F. Topputo · E. Belbruno

Computation of Weak Stability Boundaries: Sun–Jupiter System

Abstract We compute the weak stability boundary in the planar circular restricted three-body problem starting from the algorithmic definition, and its generalization by García and Gómez. In addition, we consider a new set of primaries, Sun–Jupiter, to replace the case of Earth–Moon considered in previous studies. Numerical enhancements are described and compared to previous methods. This includes defining the equations of motion in polar coordinates and a modified numerical scheme for the derivation of both stable sets and their boundaries. These enhancements decrease the computational time. New results are obtained by considering the Sun–Jupiter case which we compare to the Earth–Moon case.

1 Introduction

The concept of weak stability boundary, or equivalently WSB, was first introduced in 1986 to design low energy transfers to the Moon [1,2]. The idea was to to find a location about the Moon, in phase space, where a spacecraft could be captured ballistically, that is, with no propellant. The utilization of this region has generated new low energy transfers to the Moon, and other locations in space, as is well known, such as Japan's *Hiten*, for example. The WSB region gives rise to a sensitive dynamics about the Moon, as it defines a location that lies at the transition between lunar capture and escape. In fact, a hyperbolic network was proven to be associated to this region in the restricted three-body problem [2].

The original computation of the WSB was based on a straight forward numerical algorithm. This algorithm measures the change in stability of the motion of zero-mass point, P_3, in the restricted three-body problem, as it moves about the secondary mass point, P_2, after making

Francesco Topputo
Politecnico di Milano, Aerospace Engineering Department
Via La Masa, 34, 20156, Milan, Italy
E-mail: topputo@aero.polimi.it

Edward Belbruno
Princeton University, Department of Astrophysical Sciences
Peyton Hall, Ivy Lane, Princeton, NJ 08544, USA
E-mail: belbruno@princeton.edu

one cycle about it. The motion of P_3 is gravitationally perturbed by the primary mass point P_1, where it is assumed that the mass of P_2 is much smaller than the mass of P_1. Although this definition worked well for applications, it seemed that it could be generalized further. For example, instead of measuring the stability of motion after one cycle about P_2, why not after two or more cycles?

A satisfactory generalization of this region was published by García and Gómez in 2007 [3]. They examined the stability of motion of P_3 about P_2 after it performed n cycles. A generalized numerical algorithm was described to do this. Using this methodology, they were able to define an n-th weak stability boundary. A generalized weak stability boundary was then defined as the union of these sets for $n = 1, 2, 3, \ldots$ They did this for the case of the mass ratio of P_1, P_2 for the Earth–Moon system.

This paper has two purposes. The first is to reexamine the numerical approach in [3] by using certain modifications to enhance the numerics. These modifications include the use of polar coordinates, to compute the stable sets, and a bisection algorithm, to obtain their boundaries. We will demonstrate that these modifications allow us to compute the stable sets more efficiently and their boundaries with greater accuracy. This is demonstrated with numerical examples. The second purpose of this paper is to compute the weak stability boundary for another basic example not yet considered, the Sun–Jupiter system. In this way, insights into the mass parameter variability of the stable sets can be gained. The change of mass ratio has indeed the effect of changing the geometry of the stable sets, where new regions about P_2 are found if the Sun–Jupiter case is compared to the Earth–Moon system [3, 4]. Finally, we discuss the possible relationship of the weak stability boundary to the invariant manifolds associated to the Lyapunov orbits.

The paper is organized as follows. The planar circular restricted three-body problem and its representation in various coordinate systems, including polar coordinates, is defined below. In Section 2 a general algorithmic definition of the WSB is given and its computation is described in Section 3. The computed stable sets and WSB are presented in Section 4 for the Sun–Jupiter system for a wide class of parameter values (i.e., eccentricity and stability number). Some comments into the dynamics governing the orbits lying on the WSB are described. Concluding remarks are given in Section 5.

This paper can be viewed as a note to [3] where an additional basic example is given, using the Sun–Jupiter system, and some numerical enhancements are described.

1.1 Planar Circular Restricted Three-Body Problem

The model that we use to describe the motion of a particle of zero mass is the planar circular restricted three-body problem (or simply RTBP). In this model, relative to an inertial frame, two primary bodies P_1, P_2 of masses $m_1 >> m_2 > 0$, respectively, move under the mutual gravity on circular orbits about their common center of mass. The third body P_3, assumed to be of zero mass, moves under the gravity of the primaries in their plane of motion. In our case, P_3 represents, for example, a spacecraft, and P_1, P_2 represent Sun and Jupiter, respectively.

The motion of P_3 is studied in a rotating coordinate system with coordinates x, y and whose origin lies at the center of mass of P_1, P_2. This coordinate system rotates with the same angular velocity as P_1, P_2 about their center of mass. In this system, we can assume P_1, P_2 are fixed on the $x-$axis. Let $\mu = m_2/(m_1 + m_2)$. It is well known that we can normalize the units so that the distance between P_1, P_2 and their mutual angular velocity are both 1. Also, we can assume that P_1 is located at $(-\mu, 0)$ and P_2 is located at $(1 - \mu, 0)$, where the mass of P_1 is $1 - \mu$ and the mass of P_2 is μ. In the case of the Sun–Jupiter system $\mu = 9.538754 \, 10^{-4}$, which is assumed for the remainder of the paper [5].
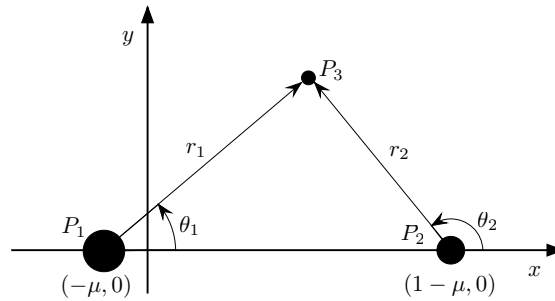
Fig. 1 Rotating reference system.

The motion of P_3 relative to the normalized co-rotating frame is described by the following system of second-order differential equations

$$\ddot{x} - 2\dot{y} = \frac{\partial \Omega}{\partial x}, \qquad \ddot{y} + 2\dot{x} = \frac{\partial \Omega}{\partial y}, \tag{1}$$

where Ω is given by

$$\Omega(x, y) = \frac{1}{2}(x^2 + y^2) + \frac{1 - \mu}{r_1} + \frac{\mu}{r_2} + \frac{1}{2}\mu(1 - \mu). \tag{2}$$

r_1 and r_2 represent the distances from P_3 to P_1 and P_2, respectively, and are given by $r_1^2 = (x + \mu)^2 + y^2$, $r_2^2 = (x + \mu - 1)^2 + y^2$ (Figure 1).

The motion described by (1) has five equilibrium points, known as the Euler–Lagrange libration points, labeled L_k, $k = 1, \ldots, 5$. Three of these, L_1, L_2, L_3, lie along the x-axis, while, L_4, L_5 lie at the vertices of two equilateral triangles with common base extending from P_1 to P_2. The RTBP admits also an integral of motion, the Jacobi integral,

$$J(x, y, \dot{x}, \dot{y}) = 2\Omega(x, y) - (\dot{x}^2 + \dot{y}^2). \tag{3}$$

Thus, each solution $\boldsymbol{x}(t) = (x(t), y(t), \dot{x}(t), \dot{y}(t))$ of (1) always lies on an energy surface

$$\mathcal{J}(C) = \{(x, y, \dot{x}, \dot{y}) \in \mathbb{R}^4 | J(x, y, \dot{x}, \dot{y}) = C\}, \tag{4}$$

for some energy C. This energy surface is a three-dimensional in the four-dimensional phase space $(x, y, \dot{x}, \dot{y}) \in \mathbb{R}^4$. The projection of the energy surface $\mathcal{J}(C)$ onto the configuration space (x, y) is called a Hill's region, and is given by

$$\mathcal{H}(C) = \{(x, y) \in \mathbb{R}^2 | 2\Omega(x, y) - C \geq 0\}. \tag{5}$$

The motion of P_3 is always confined to the Hill's region of the corresponding Jacobi energy C. The Hill's regions vary with the Jacobi energy C. Their topology changes at the values of $C = C_k$ corresponding to the libration points L_k (see [2,5] for more details).

Computing WSB implies integrating many thousands of orbits, and some of them can result in collision of P_3 with either P_1 or P_2. As a result, the numerical integration fails as the equations of motion (1) become singular for $r_{1,2} \to 0$. It is therefore necessary to regularize the equations to avoid such singularities. Levi-Citiva regularization is convenient to use. It is a local regularization method, and requires two different transformations to eliminate the singularities at both P_1 and P_2 (see [5,6] for details). We briefly summarize:

Let $\boldsymbol{z} = x + iy$ be a vector defined in the complex plane having real part x and imaginary part y, and let $\boldsymbol{w} = u + iv$ be another vector defined in the regularized complex plane (u, v). The Levi-Civita transformation that regularizes a collision at P_2 can be written as

$$\boldsymbol{z} = \boldsymbol{f}(\boldsymbol{w}) = \boldsymbol{w}^2 + 1 - \mu. \tag{6}$$

It is also necessary to transform the independent variable t to a new variable τ. This is given by

$$\frac{\mathrm{d}t}{\mathrm{d}\tau} = g(\boldsymbol{w}) = |\boldsymbol{f}'|^2 = 4|\boldsymbol{w}|^2. \tag{7}$$

It can be shown that the regularized equations of motion can be written as [5]

$$\boldsymbol{w}'' + 2i|\boldsymbol{f}'|^2\boldsymbol{w}' = \nabla_{\boldsymbol{w}}|\boldsymbol{f}'|^2 U, \tag{8}$$

where $U = \Omega - C/2$, $\nabla_{\boldsymbol{w}} = (\partial/\partial u, \partial/\partial v)$, and $(\cdot)' = \mathrm{d}/\mathrm{d}\tau$. Analogously, it can be shown that the transformation $\boldsymbol{z} = \boldsymbol{f}(\boldsymbol{w}) = \boldsymbol{w}^2 - \mu$, together with the time transformation (7), regularizes collisions with P_1.

The regularized equations of motion (8) are numerically integrated when $r_1 < r_{LC}$ or $r_2 < r_{LC}$, i.e., when P_3 enters a circle of radius r_{LC} centered at either P_1 or P_2. Outside these circles, the standard equations of motion (1) or those written in polar coordinates are used.

1.1.1 Polar Coordinates

It is convenient to use polar coordinates relative to P_2, (r_2, θ_2), in our analysis below (see Figure 1). These P_2-centered polar coordinates are related to the Cartesian coordinates through

$$x = 1 - \mu + r_2 \cos\theta_2, \qquad y = r_2 \sin\theta_2. \tag{9}$$

The pair (r_2, θ_2) defines a polar rotating reference system having the first unit vector aligned with the $P_2 P_3$ line (outward) and the second perpendicular to it (in the direction of increasing θ_2). In this reference system the equations of motion for P_3 turn out to be

$$\ddot{r}_2 - r_2 \dot{\theta}_2^2 - 2r_2\dot{\theta}_2 = (1 - \mu)\cos\theta_2\left(1 - \frac{1}{r_1^3}\right) + r_2\left(1 - \frac{1 - \mu}{r_1^3}\right) - \frac{\mu}{r_2^2},$$
$$r_2\ddot{\theta}_2 + 2\dot{r}_2\dot{\theta}_2 + 2\dot{r}_2 = (1 - \mu)\sin\theta_2\left(\frac{1}{r_1^3} - 1\right), \tag{10}$$

where r_1, the distance from P_3 to P_1, is expressed in P_2-centered polar coordinates as $r_1 = \sqrt{r_2^2 + 2r_2\cos\theta_2 + 1}$. Analogously, using the coordinates (r_1, θ_1), the equations of motion in the P_1-centered polar reference frame are

$$\ddot{r}_1 - r_1\dot{\theta}_1^2 - 2r_1\dot{\theta}_1 = \mu\cos\theta_1\left(\frac{1}{r_2^3} - 1\right) + r_1\left(1 - \frac{\mu}{r_2^3}\right) - \frac{1 - \mu}{r_1^2},$$
$$r_1\ddot{\theta}_1 + 2\dot{r}_1\dot{\theta}_1 + 2\dot{r}_1 = \mu\sin\theta_1\left(1 - \frac{1}{r_2^3}\right), \tag{11}$$

with $r_2 = \sqrt{r_1^2 - 2r_1\cos\theta_1 + 1}$. P_1-centered polar coordinates map into Cartesian coordinates through

$$x = -\mu + r_1\cos\theta_1, \qquad y = r_1\sin\theta_1. \tag{12}$$

Both systems (10) and (11) are equivalent to equations of motion (1). The polar coordinates are used in cases where the angle with respect to one of the two primaries, θ_1 or θ_2, is required as a smooth function of time. Nevertheless, when written as systems of four first-order differential equations, the vector fields generated by (10) and (11) are computationally more intensive to evaluate than the vector field associated to (1) due to the presence of trigonometric functions.

2 Definition of Weak Stability Boundary

Let H_2 be the Kepler energy of P_3 with respect to the the primary P_2. It is given by

$$H_2 = \frac{1}{2}v_2^2 - \frac{\mu}{r_2}, \tag{13}$$

where v_2 is the speed of P_3 relative to the P_2-centered inertial reference frame. We consider the case where the motion of P_3 starts from the periapsis of an osculating ellipse around P_2. In this case we have

$$r_2 = a(1-e), \qquad v_2 = \sqrt{\frac{\mu(1+e)}{r_2}}, \tag{14}$$

where a and e are the semi-major axis and the eccentricity of the osculating ellipse. Throughout the paper we consider the case where P_3 initially lies at the periapsis of a *prograde* ellipse, i.e., P_3 rotates counterclockwise in a P_2-centered inertial frame. With relations (14) the initial Kepler energy becomes

$$H_2 = \frac{1}{2}\frac{\mu(e-1)}{r_2}. \tag{15}$$

Let $\boldsymbol{x}(t)$ be a solution of (1). We say that P_3 is ballistically captured by P_2 at time t_1, if $H_2(\boldsymbol{x}(t_1)) < 0$, and it is temporary ballistically captured (or weakly captured) by P_2, if $H_2(\boldsymbol{x}(t)) < 0$ for $t_1 \leq t \leq t_2$ and $H_2(\boldsymbol{x}(t)) > 0$ for $t < t_1$ and $t > t_2$, for finite times t_1, t_2, $t_1 < t_2$. Regarding the opposite type of behavior, P_3 is ballistically ejected (or ballistically escapes) from P_2 at a time t_1 if $H_2(\boldsymbol{x}(t)) < 0$ for $t < t_1$ and $H_2(\boldsymbol{x}(t)) \geq 0$ for $t \geq t_1$. The region where weak capture occurs can be used to define the weak stability boundary. This was first defined in [1,2], and further improved in [3]. We describe the generalized version of the definition of the WSB stated in [3], with some refinements.

We consider trajectories of P_3 with the following initial conditions:

(i) The initial position of the trajectory is on a radial segment $l(\theta)$ departing from P_2 and making an angle θ with the $P_1 P_2$ line, relative to the rotating system. The trajectory is assumed to start at the periapsis of an osculating ellipse around P_2, whose semi-major axis lies on $l(\theta)$ and whose eccentricity e is held fixed along $l(\theta)$.

(ii) The initial velocity of the trajectory is perpendicular to $l(\theta)$, and the Keplerian energy H_2 of P_3 relative to P_2 is negative, i.e., $H_2 < 0$. The motion, for fixed values of the parameters θ and e, and for a choice of direction of the initial velocity vector such that a prograde osculating ellipse is achieved, depends only on the initial distance r.

(iii) The motion is said to be n-stable if the infinitesimal mass P_3 leaves $l(\theta)$, makes n complete turns about P_2, and returns to $l(\theta)$ at a point with negative Kepler energy H_2 with respect to P_2, *without* making a complete turn around P_1 along this trajectory. The motion is otherwise said to be n-unstable (Figure 2).

It is worth observing that the motion of P_3 is unstable if either P_3 performs a full circle about P_2 and returns on $l(\theta)$ on a point where $H_2 \geq 0$ or P_3 moves away from P_2 and performs a full circle about P_1. The former is a ballistic escape, the latter is said primary interchange escape [2].

We note that the n-stability condition is an open condition. This is due to the fact that $H_2 < 0$ is an open condition, and that the n-th return map to $l(\theta)$ is smooth, due to the smooth dependence of solutions of differential equations on initial conditions. Thus the set of the n-stable points on $l(\theta)$ is an open subset of $l(\theta)$, hence it is a countable union of open intervals

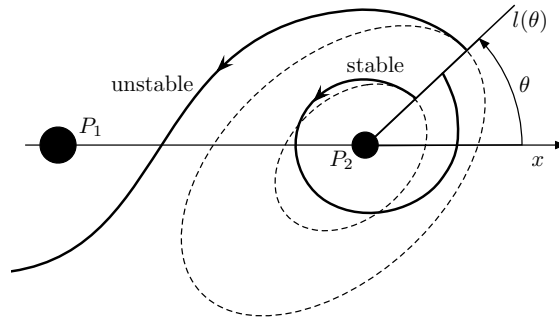$$\mathcal{W}_n(\theta, e) = \bigcup_{k \geq 1} (r_{2k-1}^*, r_{2k}^*), \tag{16}$$

Fig. 2 Example of 1-stable and unstable trajectories relative to P_2.

with $r_1^* = 0$. The points of the type r^* that are at endpoints of intervals above (except for r_1^*) are n-unstable.

For the sake of a clear exposition, we define the set $\mathcal{W}_n(e)$ obtained by varying the parameter θ and, at the same time, by holding fixed the eccentricity e

$$\mathcal{W}_n(e) = \bigcup_{\theta \in [0, 2\pi]} \mathcal{W}_n(\theta, e). \tag{17}$$

Thus, the n-stable set is

$$\mathcal{W}_n = \bigcup_{e \in [0,1)} \mathcal{W}_n(e). \tag{18}$$

This is also an open set since the n-stability of points depends smoothly on e and θ.

Definition 1 The weak stability boundary of order n, denoted by $\partial \mathcal{W}_n$ is the locus of all points $r^*(\theta, e)$ along the radial segment $l(\theta)$ for which there is a change of stability of the initial trajectory, that is, $r^*(\theta, e)$ is one of the endpoints of an interval (r_{2k-1}^*, r_{2k}^*) characterized by the fact that for all $r \in (r_{2k-1}^*, r_{2k}^*)$ the motion is n-stable, and there exist $r' \notin (r_{2k-1}^*, r_{2k}^*)$, arbitrarily close to either r_{2k-1}^* or r_{2k}^* for which the motion is n-unstable. Thus

$$\partial \mathcal{W}_n = \{r^*(\theta, e) \,|\, \theta \in [0, 2\pi], e \in [0, 1)\}.$$

Analogously, we can define a subset of the n-th weak stability boundary, $\partial \mathcal{W}_n(e)$, obtained by fixing the eccentricity of the osculating ellipse,

$$\partial \mathcal{W}_n(e) = \{r^*(\theta, e) \,|\, \theta \in [0, 2\pi]\}. \tag{19}$$

Both $\mathcal{W}_n(e)$ and $\partial \mathcal{W}_n(e)$ have been defined for illustration purposes as they have one dimension less than $\mathcal{W}_n$ and $\partial \mathcal{W}_n$, respectively.

The generalized definition of the weak stability boundary just given slightly differs from the definition given in [3] as the openness of $\mathcal{W}_n$ sets has been here considered.

3 Computation of Stable Sets and Weak Stability Boundaries

From the definition given in the previous section, both the n-stable sets, $\mathcal{W}_n$, and their weak stability boundaries, $\partial \mathcal{W}_n$, have to be determined for various values of n. We compute $\mathcal{W}_n$ first, and then its enclosure $\partial \mathcal{W}_n$. The derivation of these two sets involve the definition of a computational grid of initial conditions and the integration of hundred thousands of orbits. The first set, $\mathcal{W}_n$, is defined over a relatively coarse grid, whereas the second set is achieved on a locally refined grid in order to determine $\partial \mathcal{W}_n$ with a high level of accuracy.

3.1 Computation of $\mathcal{W}_n$

To accomplish this task it is necessary to integrate a large number of orbits and to keep track of those that are n-stable. An initial condition is uniquely specified once the triple (r, θ, e) is given. The initial condition to flow under dynamical system (1) is indeed

$$
\begin{aligned}
x &= r \cos \theta + 1 - \mu, & y &= r \sin \theta, \\
\dot{x} &= -v \sin \theta + r \sin \theta, & \dot{y} &= v \cos \theta - r \cos \theta,
\end{aligned}
\tag{20}
$$

with $v = \sqrt{\mu(1+e)/r}$. The associated orbits have to be integrated for a large time span in order to assess wether the orbit is stable or not. In [3], an interval of 80 adimensional units has been used. Instead of assuming a fixed final time, in this work we use a different methodology that allows us to get the final time in an automatic way, depending on the orbit being integrated. In this section we show that this method requires the orbits to be integrated for a much shorter time.

We recall that the orbits are taken on a radial line $l(\theta)$ emanating from P_2 and making an angle of θ with the x-axis. Using P_2-centered polar coordinates (r_2, θ_2) introduced in Section 1.1.1, and the associated equations of motion (10), is a more natural choice to derive $\mathcal{W}_n$ sets. Indeed, integrating the system in polar coordinates allows us to handle the angle θ_2 as a smooth function of time, $\theta_2 = \theta_2(t)$ (discontinuous inverse trigonometric functions are involved if θ_2 is derived inverting equations (9)). By tracking this angle during the integration, we are able to establish wether P_3 makes a complete turn about P_2 or not. We say in fact that P_3 completes a full turn about P_2 at time t^* if

$$
|\theta_2(t^*) - \theta_2(t_0)| = 2\pi,
\tag{21}
$$

for the smallest $t^* > t_0$ such that (21) is verified (t_0 is the initial time). Using instead the P_1-centered polar coordinates (r_1, θ_1), it is possible to define the condition for a primary interchange escape to occur in a totally analogous fashion. We say that P_3 performs a primary interchange escape at time t^* if

$$
|\theta_1(t^*) - \theta_1(t_0)| = 2\pi.
\tag{22}
$$

Thus, the numerical integration terminates at $t = t^*$, i.e., when at least one of the two conditions above is verified for the first time. The time span for integration is therefore $[t_0, t^*]$. Numerical experiments show that $t^* \ll 80$ for all orbits considered (see Figure 3(b) where the t^* values are reported for $\mathcal{W}_1(0.0)$). If condition (21) is verified (and the orbit is such that $H_2(t^*) < 0$) the motion is stable, otherwise, if condition (22) is satisfied, the orbit is unstable. (There are certain cases where the two conditions are satisfied simultaneously; in these cases the orbits are judged unstable.) Thus, in order to assess the stability of the motion, both θ_1 and θ_2 have to be handled as a smooth function of time. This is possible by *simultaneously* integrating the two systems (10) and (11) with initial conditions

$$
\begin{aligned}
r_2(t_0) &= r, & \theta_2(t_0) &= \theta, \\
\dot{r}_2(t_0) &= 0, & \dot{\theta}_2(t_0) &= \sqrt{\frac{\mu(1+e)}{r^3}} - 1,
\end{aligned}
\tag{23}
$$

for system (10) and

$$
\begin{aligned}
r_1(t_0) &= \sqrt{r^2 + 2r \cos \theta + 1}, \quad \theta_1(t_0) = \tan^{-1}\left(\frac{r \sin \theta}{1 + r \cos \theta}\right), \\
\dot{r}_1(t_0) &= \dot{r}_2(t_0) \cos(\theta - \theta_1(t_0)) - r_2(t_0)\dot{\theta}_2(t_0) \sin(\theta - \theta_1(t_0)), \\
\dot{\theta}_1(t_0) &= \frac{\dot{r}_2(t_0)}{r_1(t_0)} \sin(\theta - \theta_1(t_0)) + \frac{r_2(t_0)\dot{\theta}_2(t_0)}{r_1(t_0)} \cos(\theta - \theta_1(t_0)),
\end{aligned}
\tag{24}
$$

for system (11). Integrating the coupled system of equations (10)–(11) is much more computational intensive than simply flowing equations (1). Nevertheless, as clearly shown in Table 1, integrating the coupled system (10)–(11) with a variable final time, determined by either condition (21) or (22), is a more efficient choice than integrating (1) for a fixed, long time span.

The coupled initial conditions (23)–(24) still depend on the triple (r, θ, e). These three parameters are defined on the grid

$$
\begin{aligned}
r &= \{0, \ 2\,10^{-3}, \ \ldots, \ 1.5\}, \\
\theta &= \{0, \ 2\pi/1000, \ \ldots, \ 2\pi\}, \\
e &= \{0, \ 0.05, \ \ldots, \ 0.95\},
\end{aligned}
\tag{25}
$$

and three nested loops are necessary to describe all their combinations. About $7.5\,10^5$ integrations are needed to generate each $\mathcal{W}_n(e)$, whereas the whole $\mathcal{W}_n$ sets can be obtained with $1.5\,10^7$ integrations. A 7th–8th order Runge–Kutta–Fehlberg integration scheme implemented in Matlab is used to flow system (10)–(11). When P_3 enters either of the two circles $r_{1,2} < r_{LC}$, the state is transformed into Cartesian coordinates and then, through equation (6) (or the equivalent form for regularizing impacts with P_1) it is mapped into the regularized variables (u, v). Regularized system (8) is used in this region until P_3 reaches the boundary $r_{1,2} = r_{LC}$. In this paper we have taken $r_{LC} = 10^{-3}$.

In Figure 3(a) we have reported the set $\mathcal{W}1(0.0)$ generated through the computational grid defined in (25) with the eccentricity held fixed to zero. The 1-stable set is made up by $2.8\,10^4$ points, out of the $7.5\,10^5$ integrated orbits. Among these orbits, a total of $3.6\,10^3$ has required a regularization of the dynamics (black points in Figure 3(a)). If either the Cartesian or polar equations of motions were used to flow such points, the numerical integration would have either failed or required a long computational time. The inclusion of a regularization strategy is therefore crucial for the derivation of the stable sets as a relative high number of initial conditions result in either collision or close encounter with P_2.

In Figure 3(b) the integration times, t^*, in equation (21) have been reported for the orbits making up $\mathcal{W}_1(0.0)$. The orbits with final integration times differing by less than 5 adimensional units have been grouped in subsets for the sake of exposition. It can be observed that the vast majority of stable orbits perform a loop about P_2, or equivalently verify equation (21), in much less than 80 time units. More specifically, 95% of the stable orbits have a final integration time less than 10 units, and even no stable orbits with t^* grater than 65 units have been found.

Table 1 reports a comparison of the CPU time required for the derivation of various $\mathcal{W}_1(e)$ sets with increasing eccentricity. The method described so far (i.e., coupled integration of systems (10) and (11) together with stopping conditions (21) and (22)) is compared with the integration of Cartesian equations of motion for 80 time units. The advantages of having introduced a method based on polar coordinates over the method described in [3] are evident.

3.2 Computation of $\partial\mathcal{W}_n$

Once the stable sets $\mathcal{W}_n$ have been computed, for fixed values of (θ_i, e_j) on the discrete grid (25), there are one or more boundary points on $\mathcal{W}_n$, $r^s = r(\theta_i, e_j)$, such that either $r(\theta_i, e_j) + \Delta r$ or $r(\theta_i, e_j) - \Delta r$ is an unstable point ($\Delta r = 2\,10^{-3}$ in agreement with the grid defined in (25)). In the following we consider the case where r^s is an exterior boundary of $\mathcal{W}_n(e_j)$, i.e., $r^u = r^s + \Delta r$ is unstable; extending the method to interior stable points is trivial.

The stable sets $\mathcal{W}_n(e_j)$ have been obtained on the relatively coarse grid (25). The focus now is the fine determination of the weak stability boundaries $\partial\mathcal{W}_n(e_j)$ on a dynamically refined grid. We first assume that there is only one point of the type r^* (see equation (16)) within the interval $[r^s, \ r^u]$. This can be claimed as Δr in (25) is reasonably small, and it is verified by numerical

(a) $\mathcal{W}_1(0.0)$: regularized orbits.

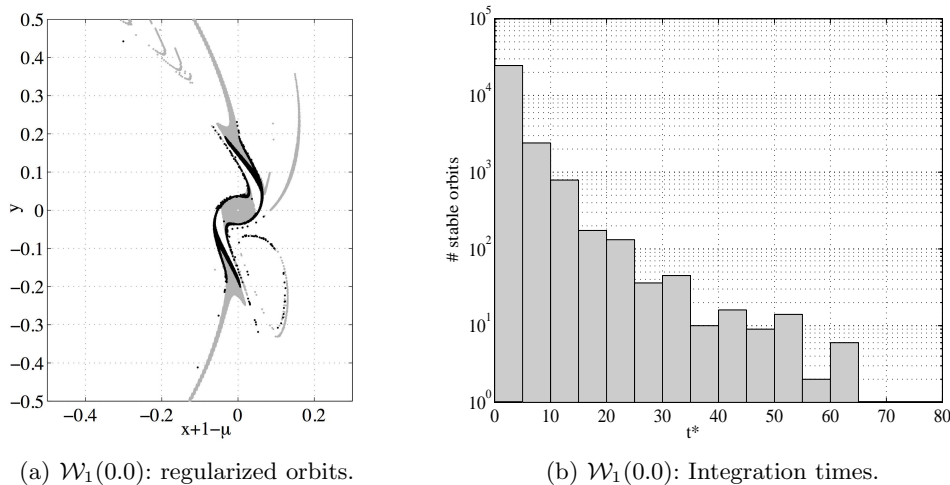(b) $\mathcal{W}_1(0.0)$: Integration times.

Fig. 3 A preliminary view of the $\mathcal{W}_1(0.0)$ set derived over the grid (25). In Figure 3(a) the black points stand for the initial conditions that generate orbits requiring a regularization of the dynamics. The integration times, t^*, are reported in Figure 3(b) versus the number of stable orbits.

	CPU time (polar)	CPU time (Cartesian)	# stable orbits	# regularized orbits
$\mathcal{W}1(0.0)$	27.3 h	132.2 h	28212	3612
$\mathcal{W}1(0.2)$	27.4 h	132.8 h	24035	4119
$\mathcal{W}1(0.4)$	27.6 h	130.3 h	18816	4230
$\mathcal{W}1(0.6)$	27.8 h	127.0 h	14479	4815
$\mathcal{W}1(0.8)$	29.7 h	125.7 h	10719	4257
$\mathcal{W}1(0.95)$	29.8 h	122.3 h	9106	3180

Table 1 Computational time required to construct the stable sets integrating the equations of motion in polar and Cartesian coordinates. Both codes are written in Matlab language. The CPU time is relative to a Dual Xeon 2.33 GHz platform running Linux. Integration tolerance is set to 10^{-14}.

experiments. Nevertheless, as the stable sets may possess a Cantor-like structure, it may occur that more than one r^* point exists within the interval $[r^s, r^u]$; this case is not considered in the derivation of the weak stability boundaries.

We implement a bisection method on the interval $[r^s, r^u]$. The midpoint of the interval, $r_k = (r^s + r^u)/2$ is in fact taken as a new starting point, and the following initial condition is flown

$$r_2(t_0) = r_k, \qquad \theta_2(t_0) = \theta_i,$$
$$\dot{r}_2(t_0) = 0, \qquad \dot{\theta}_2(t_0) = \sqrt{\frac{\mu(1+e_j)}{r_k^3}} - 1. \tag{26}$$

If (26) generates a stable orbit, then the new stable point is set to $r^s = r_k$, otherwise, if (26) results in an unstable orbit, the new unstable initial condition is updated, i.e., $r^u = r_k$. In any case the bisection method is repeated on the updated, half-size interval $[r^s, r^u]$. In our implementation, iterations go on until the last interval has amplitude $|r^u - r^s| \leq 10^{-8}$. The midpoint of this last interval is assumed to be the point on the weak stability boundary. The whole process is repeated for all (θ_i, e_j) defined on the grid (25). In this way we reach an elevate

(a) $\mathcal{W}_1(0.0)$ and $\partial\mathcal{W}_1(0.0)$.

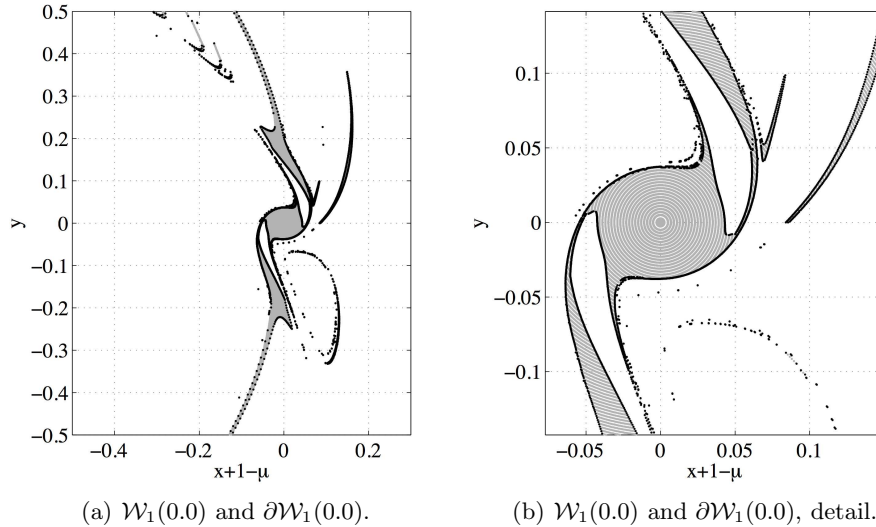(b) $\mathcal{W}_1(0.0)$ and $\partial\mathcal{W}_1(0.0)$, detail.

Fig. 4 Weak stability boundary $\partial\mathcal{W}_1(0.0)$ (black points) and 1-stable set $\mathcal{W}_1(0.0)$ (gray points). The refined weak stability boundary is obtained by application of the bisection method at the boundaries of the coarse grid where $\mathcal{W}_1(0.0)$ is defined. In Figure 4(b) the structure of this grid can be appreciated.

accuracy in the determination of $\partial\mathcal{W}_n$ since the maximum error in radial distance from P_2 is of the order of 10^{-9}.

The bisection method described above is computationally intensive and has a slow (linear) convergence. Nevertheless, this method is effective in the chaotic regions of the phase space where the weak stability boundary is defined. Furthermore, the high precision reached in the determination of $\partial\mathcal{W}_n$ will serve, in future works, to demonstrate the relations between these sets and the invariant manifolds of the Lyapunov orbits about both L_1 and L_2. The weak stability boundary $\partial\mathcal{W}_1(0.0)$, associated to the set $\mathcal{W}_1(0.0)$ shown in Figure 3(a), is reported in Figure 4.

4 Visualization of Stable Sets and Weak Stability Boundaries

The computed n-stable sets, $\mathcal{W}_n$, and their weak stability boundaries, $\partial\mathcal{W}_n$, are illustrated in this section for various values of stability number and eccentricity.

4.1 Visualization of $\mathcal{W}_n$

A sample subset of all achieved $\mathcal{W}_n$ is shown for brevity sake. Figure 5 reports the 1-stable sets $\mathcal{W}_1(e)$, $e = \{0, 0.2, 0.4, 0.6, 0.8, 0.95\}$, in the P_2-centered, co-rotating frame introduced in Section 1.1. The picture shows 1-stable initial conditions that are highlighted according to the associated Jacobi energy C, reported on the right sidebar. As observed in [3], the set of 1-stable points recalls a Cantor set; i.e., for a fixed value of e, along the line $l(\theta)$ there are different transitions from stability to instability. This is more evident for increasing eccentricities. It can be appreciated how the region about P_2 shrinks and, at the same time, becomes more irregular for $e \to 1$. In Figure 6 we have reported the n-stable sets $\mathcal{W}_n(e)$, $n = \{1, 2, \ldots, 8\}$, $e = 0$. It is straightforward that, for fixed eccentricity, $\mathcal{W}_n(e) \subseteq \mathcal{W}_m(e)$, $n \geq m$. It can be observed that the two branches of $\mathcal{W}_1(0.0)$ that are far from P_2 suddenly disappears in the other sets $\mathcal{W}_{n\geq 2}(0.0)$,
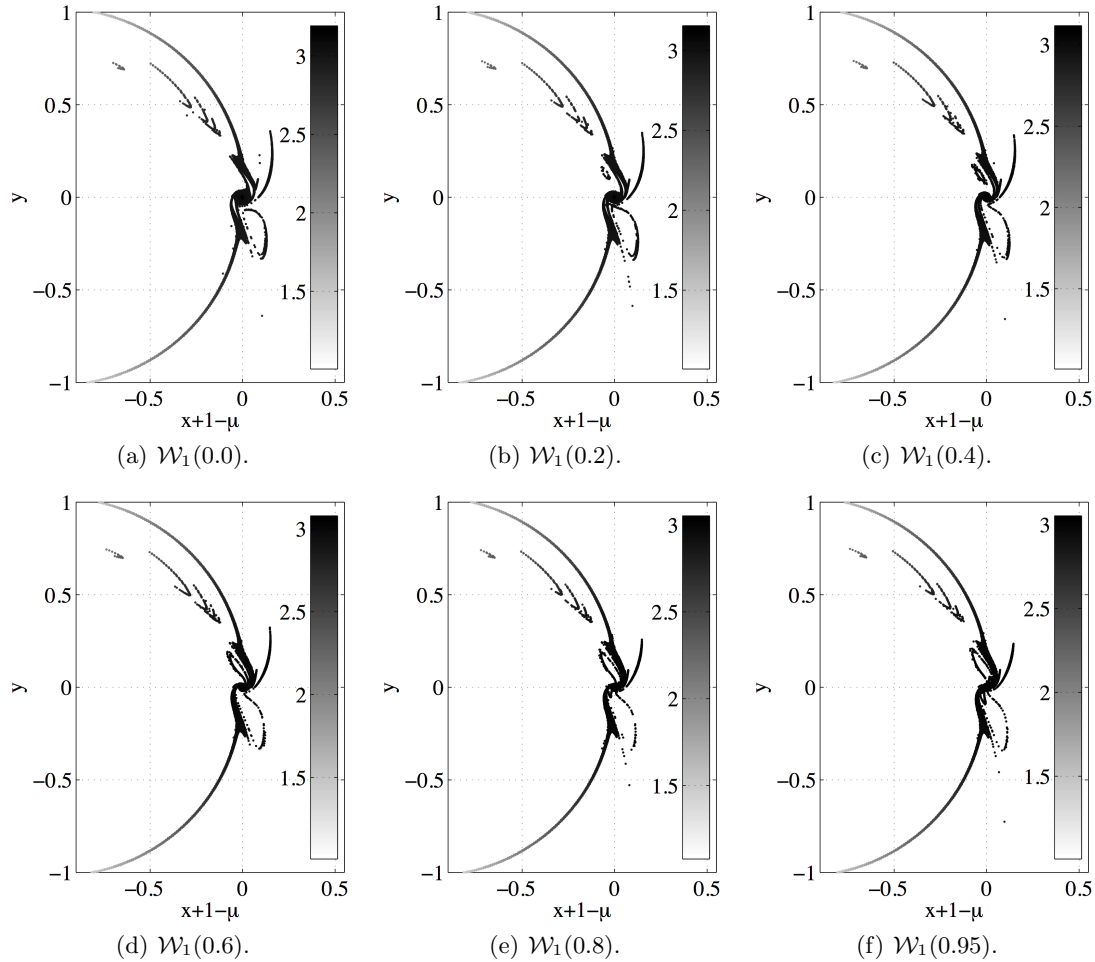
Fig. 5 Collection of $\mathcal{W}_1(e)$ sets for $e = \{0,\ 0.2,\ 0.4,\ 0.6,\ 0.8,\ 0.95\}$. The sidebar on the right reports the Jacobi energy C of the 1-stable initial conditions.

whereas the closer branches becomes thinner for increasing n. Nevertheless, the *core* of $\mathcal{W}_1(0.0)$, i.e., the quasi-circular region about P_2 (see Figures 6(a) to 6(h)), is conserved in the subsequent $\mathcal{W}_{n\geq 2}(0)$ sets. This indicates that the n-stable sets contain part of the invariant tori surrounding P_2 already observed in [7] for fixed values of C. This property can be summarized by stating that, in principle, $\mathcal{W}_n$ sets are "quasi-invariant" objects for the dynamics: they are regions in the phase space where orbits stay for a long period of time before leaving for other regions.

4.2 Visualization of $\partial\mathcal{W}_n$

The weak stability boundaries, $\partial\mathcal{W}_n(e)$, corresponding to $\mathcal{W}_n(e)$ sets discussed previously are shown. In Figure 4 the weak stability boundary $\partial\mathcal{W}_1(0.0)$ of the 1-stable set $\mathcal{W}_1(0.0)$ is reported. $\partial\mathcal{W}_1(0.0)$ has been obtained with the bisection method described in Section 3.2. In Figure 7(a), $\partial\mathcal{W}_1(e)$ sets, $e = \{0, 0.2, \ldots, 0.8, 0.95\}$, associated to the $\mathcal{W}_1(e)$ sets shown in Figure 5 are presented with e on the z-axis. In analogy with the stable sets $\mathcal{W}_1(e)$, their boundaries are more and more irregular for increasing eccentricity. In Figure 7(b) the weak stability boundary
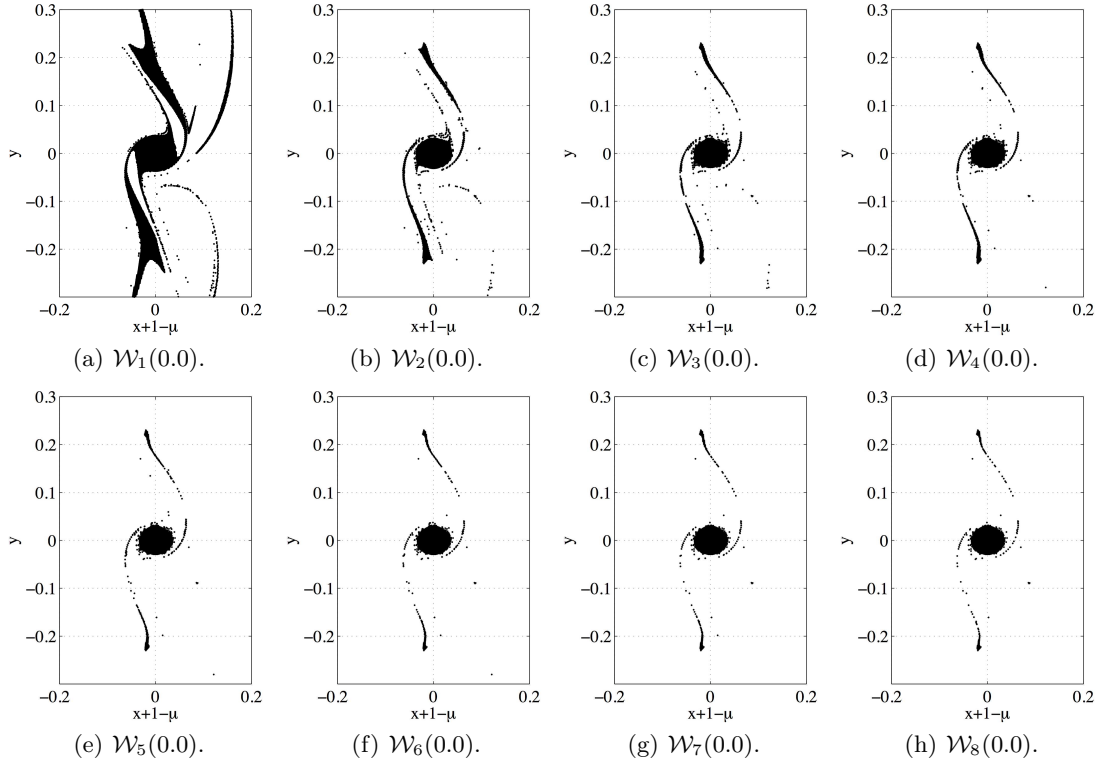
(a) $\mathcal{W}_1(0.0)$.   (b) $\mathcal{W}_2(0.0)$.   (c) $\mathcal{W}_3(0.0)$.   (d) $\mathcal{W}_4(0.0)$.

(e) $\mathcal{W}_5(0.0)$.   (f) $\mathcal{W}_6(0.0)$.   (g) $\mathcal{W}_7(0.0)$.   (h) $\mathcal{W}_8(0.0)$.

Fig. 6 Collection of $\mathcal{W}_n(e)$, $n = \{1, 2, \ldots, 8\}$, $e = 0$. It can be seen that the central structure of $\mathcal{W}_1(0.0)$ is preserved in the subsequent $\mathcal{W}_{n \geq 2}(0.0)$ sets. This indicates that the region of $\mathcal{W}_n(e)$ about P_2 is made up by invariant tori at different values of C.

(a) $\partial\mathcal{W}_1(e)$, $e = \{0, 0.2, \ldots, 0.8, 0.95\}$.   (b) $\partial\mathcal{W}_n(0.0)$, $n = \{1, 2, \ldots, 8\}$.
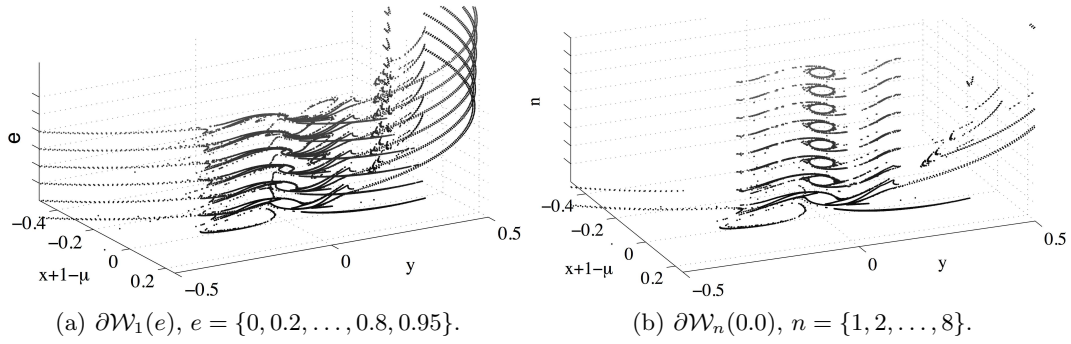
Fig. 7 Figure 7(a): $\partial\mathcal{W}_1(e)$, $e = \{0, 0.2, \ldots, 0.8, 0.95\}$, as boundaries of the 1-stable sets $\mathcal{W}_1(e)$, shown in Figure 5. Figure 7(b): $\partial\mathcal{W}_n(0.0)$, $n = \{1, 2, \ldots, 8\}$, as boundaries of the n-stable sets $\mathcal{W}_n(0.0)$, shown in Figure 6.

$\partial\mathcal{W}_n(0.0)$, $n = \{1, 2, \ldots, 8\}$, associated to the n-stable sets of Figure 6 are shown with the stability number n on the z-axis. As in Figure 6, the central structure is preserved in $\partial\mathcal{W}_n(0.0)$ as well. This indicates that, as observed for the n-stable sets, the weak stability boundaries are quasi-invariant objects for the motion of P_3.

(a) $\mathcal{W}_1(0.2)$, Sun–Jupiter.　　　　　(b) $\mathcal{W}_1(0.2)$, Earth–Moon.
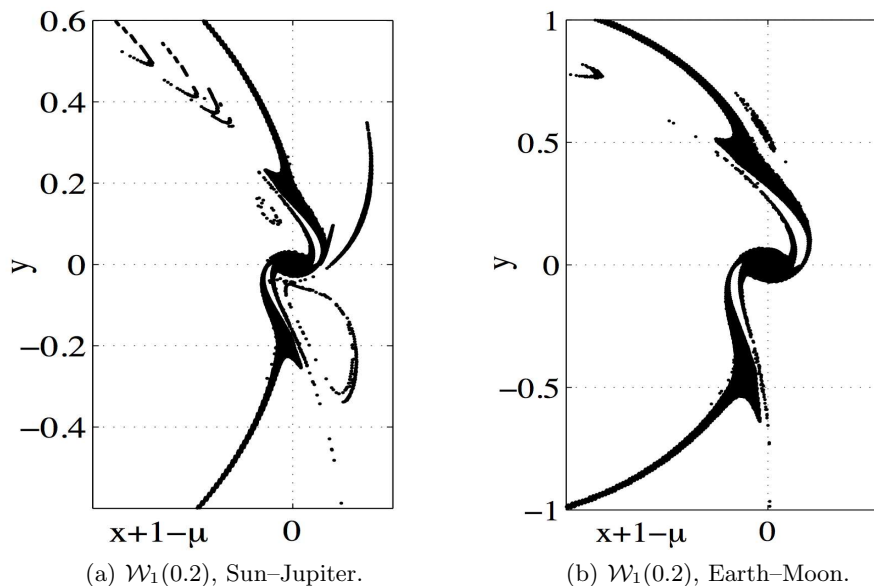
Fig. 8 The set $\mathcal{W}_1(0.2)$ in Sun–Jupiter (left) and Earth–Moon (right) systems.

4.3 Comparison with the Earth–Moon System

The stable sets and their weak stability boundaries achieved in the Sun–Jupiter system ($\mu = 9.538754\,10^{-4}$) can be compared to those defined in the Earth–Moon system ($\mu = 1.21506683\,10^{-2}$). It is indeed clear that these sets depend on the mass ratio of the three-body system, as this is the only parameter characterizing differential equations (1). Plots reported in Figures 4–6 can be compared to the visualizations in [3], where the Earth–Moon system has been investigated. As a sample comparison, we have reported in Figure 8 the set $\mathcal{W}_1(0.2)$ defined in both systems.

Not surprisingly, the scale changes, and the relative size of the two sets is different as the Earth–Moon mass ratio is about 12 times greater than the Sun–Jupiter one. Nevertheless, the dependence of the stable sets geometry on the mass ratio is not straightforward. By comparing Figures 8(a) and 8(b), it can be seen that the island on the upper right in the Earth–Moon system disappears, and branches occur in the Sun–Jupiter system (right part) that are not present in the Earth–Moon. Moreover, there are substantially new arcs in the upper left part of the Sun–Jupiter $\mathcal{W}_1(0.2)$ set. Overall, besides these changes, the two regions are qualitatively similar, although there is evidence that the smaller mass ratio is, the richer the stable sets are — which is not trivial.

5 Conclusions

In this paper we have presented a methodology to compute and visualize weak stability boundaries that is a refinement of [3], and also for a new fundamental case, the Sun–Jupiter problem. To make the existing methodology more efficient, a set of differential equations is written in polar coordinates, together with the formulation of a stop condition that allows us to significantly reduce the effort required to derive the stable sets. In addition, a bisection algorithm has been formulated for the fine definition of the weak stability boundaries. We have also found that the mass ratio variability produces important changes in the geometry of the stable sets, as the Sun–Jupiter case is different from the Earth–Moon one.
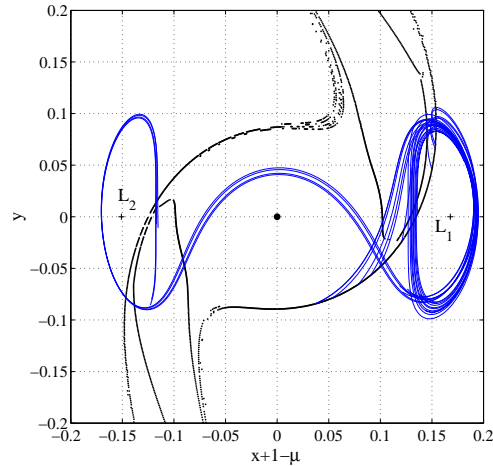
Fig. 9 A portion of $\partial\mathcal{W}_1(e)$, $e = 0$, and a set of sample orbits produced by taking random points with $\theta \in [-\pi/4, \pi/4]$ as initial conditions. There is evidence that these orbits shadow the stable manifolds of the Lyapunov orbits about both L_1 and L_2 (shown with '+' markers).

It is well known that the weak stability boundary plays a key role in the design of low energy transfers as first demonstrated in [1,2] and more recently shown in [4]. More significantly, however, this object seems to play a key role in the dynamics of motion of P_3 about P_2. It is seen that $\partial\mathcal{W}_n$ is not an invariant object, which makes its study more difficult. It also allows the dynamics of motion of P_3 about P_2 to be studied without directly analyzing the dynamics associated with the invariant manifolds associated with the Lyapunov orbits. The weak stability boundary is described by a relatively simple algorithmic definition. Nevertheless, there is evidence that it is a dynamically rich set that deserves more attention.

As a final example, we show in Figure 9 a portion of $\partial\mathcal{W}_1(e)$, $e = 0$, in the Earth–Moon system. We have taken random initial conditions for $\theta \in [-\pi/4, \pi/4]$, and we have numerically integrated these initial points under the RTBP dynamics (1). There is evidence that the orbits produced by these points shadow that stable manifolds of the Lyapunov orbits about both L_1 and L_2. Ongoing work by the same authors is indeed aimed at demonstrating that, for a significant range of energies such that the Lyapunov orbits exist, a portion of the weak stability boundaries locally overlap with the invariant manifolds of the Lyapunov orbits about both L_1 and L_2.

Acknowledgement

References

1. Belbruno, E. and Miller, J., Sun-Perturbated Earth-to-Moon Transfers with Ballistic Capture, Journal of Guidance, Control and Dynamics, 16, 770–775 (1993).
2. Belbruno E., Capture Dynamics and Chaotic Motions in Celestial Mechanics, Princeton University Press, Princeton (2004).
3. García, F. and Gómez, G., A Note on Weak Stability Boundaries, Celestial Mechanics and Dynamical Astronomy, 97, 87–100 (2007).

4. Romagnoli, D. and Circi, C., Earth–Moon Weak Stability Boundaries in the Restricted Three and Four Body Problem, Celestial Mechanics and Dynamical Astronomy, 103, 79–103 (2009).
5. Szebehely, V., Theory of Orbits: The Restricted Problem of Three Bodies, Academic Press Inc., New York (1967).
6. Celletti, A., Basics of Regularization Theory, in Chaotic Worlds: From Order to Disorder in Gravitational N-Body Dynamical Systems, Springer Netherlands, 203–230 (2006).
7. Belbruno, E., Topputo, F., and Gidea, M., Resonance Transitions Associated to Weak Capture in the Restricted Three-Body Problem, Advances in Space Research, 42, 1330–1351 (2008).